INTERNATIONAL JOURNAL OF
Minerals, Metallurgy and Materials

Volume 31, Number 2, February 2024
Page 323

Research Article https://doi.org/10.1007/s12613-023-2736-0

Flow characteristics and hot workability of a typical low-alloy high-strength steel during multi-pass deformation

Mingjie Zhao[1,2], *Lihong Jiang*[1], *Changmin Li*[3], *Liang Huang*[3],✉, *Chaoyuan Sun*[4], *Jianjun Li*[3,5], *and Zhenghua Guo*[1],✉

1) School of Aeronautical Manufacturing Engineering, Nanchang Hangkong University, Nanchang 330063, China
2) Jiangxi Key Laboratory of Forming and Joining Technology for Aerospace Components, Nanchang Hangkong University, Nanchang 330063, China
3) State Key Laboratory of Materials Processing and Die & Mould Technology, School of Materials Science and Engineering, Huazhong University of Science and Technology, Wuhan 430074, China
4) China National Erzhong Group Deyang Wanhang Die Forging Co. LTD., Deyang 618000, China
5) Hubei Huangshi Mold Industrial Technology Research Institute, Huangshi 435007, China

(Received: 29 June 2023; revised: 16 August 2023; accepted: 30 August 2023)

Abstract: Heavy components of low-alloy high-strength (LAHS) steels are generally formed by multi-pass forging. It is necessary to explore the flow characteristics and hot workability of LAHS steels during the multi-pass forging process, which is beneficial to the formulation of actual processing parameters. In the study, the multi-pass hot compression experiments of a typical LAHS steel are carried out at a wide range of deformation temperatures and strain rates. It is found that the work hardening rate of the experimental material depends on deformation parameters and deformation passes, which is ascribed to the impacts of static and dynamic softening behaviors. A new model is established to describe the flow characteristics at various deformation passes. Compared to the classical Arrhenius model and modified Zerilli and Armstrong model, the newly proposed model shows higher prediction accuracy with a confidence level of 0.98565. Furthermore, the connection between power dissipation efficiency (PDE) and deformation parameters is revealed by analyzing the microstructures. The PDE cannot be utilized to reflect the efficiency of energy dissipation for microstructure evolution during the entire deformation process, but only to assess the efficiency of energy dissipation for microstructure evolution in a specific deformation parameter state. As a result, an integrated processing map is proposed to better study the hot workability of the LAHS steel, which considers the effects of instability factor (IF), PDE, and distribution and size of grains. The optimized processing parameters for the multi-pass deformation process are the deformation parameters of 1223–1318 K and 0.01–0.08 s^{-1}. Complete dynamic recrystallization occurs within the optimized processing parameters with an average grain size of 18.36–42.3 μm. This study will guide the optimization of the forging process of heavy components.

Keywords: low-alloy high-strength steel; work hardening rate; constitutive model; hot workability; multi-pass deformation

1. Introduction

Low-alloy high-strength (LAHS) steels are popular in manufacturing heavy components due to their low cost and superior performance [1–3]. Due to the complex structure, huge size, and large deformation resistance, heavy components of LAHS steels are usually formed by multi-pass forging [4–5]. However, the deformation behaviors and hot workability of metallic materials during the multi-pass deformation process are different from those of the single-pass deformation process [6–8]. Because the static softening mechanisms may occur during the multi-pass deformation process [9–11]. In order to realize the accurate regulation of the deformation behaviors of the LAHS steels during the multi-pass forging process of heavy components, it is necessary to carry out research on the flow characteristics and hot workability during the multi-pass deformation process.

There are many studies on the multi-pass deformation of metallic materials [12–15]. Liu *et al.* [16] found that the main softening mechanisms of Ti–6Al–4V alloy during various deformation passes are the dynamic recrystallization (DRX) of β phase for the first-pass deformation, spheroidization of α phase for the second-pass deformation, and DRX of α phase for the third-pass deformation. Ma *et al.* [17] found that the mechanism for the static softening of TA15 alloy is the globularization behavior of the primary α phase. Tang *et al.* [18] proposed an integrated model to evaluate the impacts of different alloying elements on the static softening behaviors of Al–Zn–Mg–Cu alloys. Jia *et al.* [19] established a density-based model for the flow stress of Q345B steel during the multi-pass deformation process, which considered the influences of dynamic and static softening mechanisms. Wang

---

✉ Corresponding authors: Liang Huang E-mail: huangliang@hust.edu.cn; Zhenghua Guo E-mail: guozhenghua@nchu.edu.cn

et al. [20] established a multi-scale model, and simulated the macro and micro evolution during the multi-pass deformation process. Nie *et al.* [21] established processing maps of Mg–8Gd–3Y under multi-pass deformation, and pointed out that processing windows can be widened by multi-pass deformation.

During the multi-pass deformation process, dynamic and static softening mechanisms are complex, which can affect the deformation behaviors under various deformation passes [22–23]. Reliable constitutive models and reasonable processing parameters can ensure the accurate prediction and effective regulation of deformation behaviors of metallic materials during the multi-pass deformation process. However, current constitutive models for multi-pass deformation are complex, which restricts their application in commercial software. It is significant to establish a concise and reliable constitutive model for multi-pass deformation. Furthermore, the current optimization method of processing maps is based on instability factor (IF) and peak power dissipation efficiency (PDE). Actually, peak PDE does not always correspond to the optimal interval of deformation parameters. How to accurately optimize the processing parameter interval is an urgent problem to be solved.

For the hot deformation behaviors of LAHS steels, Li *et al.* [24] investigated the DRX mechanism of 300M steel and constructed a DRX kinetics model. Xiong *et al.* [25] constructed a model for the flow stress of ultrahigh-strength steel during single-pass deformation. Wang *et al.* [26] explored the hot workability of 30Si2MnCrMoVE steel during the single-pass deformation process. Zhao *et al.* [27] explored the metadynamic recrystallization mechanism of 300M steel by *in-situ* observations. Chen *et al.* [28] analyzed the impacts of deformation temperature, strain rate, strain, inter-pass soaking time, and deformation passes on the flow stress. However, there are few reports on the constitutive analysis and evaluation of hot workability for the multi-pass deformation of LAHS steels. As mentioned above, the deformation behaviors of the multi-pass deformation process are significantly different from those of the single-pass deformation process. It is vital to explore the deformation behaviors of LAHS steels during multi-pass deformation.

In the study, the multi-pass compression experiments are carried out on the Gleeble 3500 device to mimic the multi-pass forging process of LAHS steels. The impacts of deformation parameters and passes on work hardening behaviors are analyzed. A new model for flow stress during the multi-pass deformation process is established. Furthermore, a novel optimization method for the processing parameters of LAHS steels during multi-pass deformation is proposed. It is useful for the regulation of the deformation behaviors of LAHS steels during the actual multi-pass forging process.

2. Experimental

In this study, LAHS steel was used to conduct the multi-pass compression experiments by thermal simulation experiments. The LAHS steel was produced by vacuum induction melting and vacuum arc remelting, and the as-received LAHS steel was hot rolled with a diameter of 300 mm, which was provided by China National Erzhong Group Co. Table 1 depicts the chemical composition of the experimental LAHS steel. Fig. 1 displays the microstructure of the experimental LAHS steel, which consists of equiaxed grains.

Table 1. Chemical composition of the experimental LAHS steel wt%

C	Si	Mn	P	Cr	Mo	Ni	V	Cu	Fe
0.39	1.60	0.70	0.01	0.89	0.40	1.80	0.07	0.06	bal.

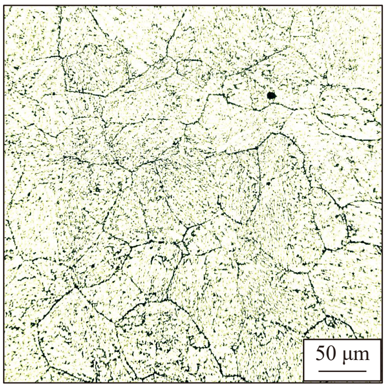

Fig. 1. Original microstructure of the experimental LAHS steel.

The multi-pass compression experiments were conducted on the Gleeble 3500 thermal simulator. The detailed principle of the experimental setup was described in the reported literature [29]. The thermal compression samples were machined to a diameter of 8 mm and height of 12 mm by the method of low-speed wire cutting. Before the thermal compression experiments, each end of the samples was placed a thin graphite film to eliminate the effect of friction. Besides, the thin tantalum sheet was placed between the graphite sheet and the indenter to prevent adhesion when the deformation amount was large. The thermocouple was welded to the middle of the samples to achieve accurate temperature control. The experimental deformation parameters were 1173–1473 K and 0.01–10 s^{-1}. Both the first-pass and second-pass strains were 0.6. The experimental procedure for thermal simulation experiments is displayed in Fig. 2. The experimental samples will be quenched quickly after the deformation process. The microstructures of experimental samples at various deformation parameters were analyzed by etching the samples. The etching method was described in the reported literature [30].

3. Results and discussion

3.1. Flow behaviors analysis

3.1.1. Stress–strain curves

Fig. 3 shows the flow stress curves at various deformation parameters. At different deformation passes, the flow stress increases as the deformation temperature falls and the strain

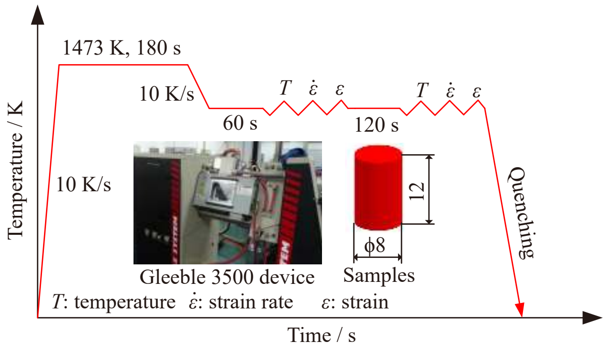

Fig. 2. Experimental procedure of thermal simulation experiments.

rate rises. It can be ascribed to the completion between the hardening effect of strain rate and the softening effect of deformation temperature. Furthermore, the stress–strain curves display peak stress during various deformation passes at high deformation temperatures and low strain rates, such as the deformation parameters of 1473 K and 0.01 s^{-1}. It indicates that it is easy for DRX development under these deformation conditions. In a comparison of flow stress among various deformation passes, the flow stress of second-pass deformation exceeds that of first-pass deformation. It can be attributed to the strain storage energy in the experimental material. The deformation amount of the first-pass deformation is not enough large to allow sufficient occurrence of DRX within the material. As a result, there is much strain storage energy in the deformed material after first-pass deformation, which causes a large deformation resistance during second-pass deformation.

3.1.2. Work hardening characteristics

According to Fig. 3, the variation rule of flow stress is distinctly various at different deformation parameters and deformation passes. In this section, the impacts of deformation parameters and passes on the variation rules of flow stress will be evaluated by the work hardening rate. The work hardening rate can be calculated by Eq. (1) [31–32]:

$$\theta = \frac{d\sigma}{d\varepsilon} \tag{1}$$

where θ is work hardening rate, σ is true stress, and ε is true strain.

The work hardening rate at various deformation conditions is calculated by Eq. (1), and Fig. 4 displays the calculated results. The work hardening rate is sensitive to the deformation conditions. As the strain rate reduces and the deformation temperature increases, the work hardening rate decreases drastically. The dislocation slip and climb can easily recombine at high deformation temperatures, promoting the production of dislocation cells and subgrains. Also, there is a longer time for element migration and the formation of DRX grains at lower strain rates. Comparing the work hardening rates at various deformation passes, the second-pass deform-

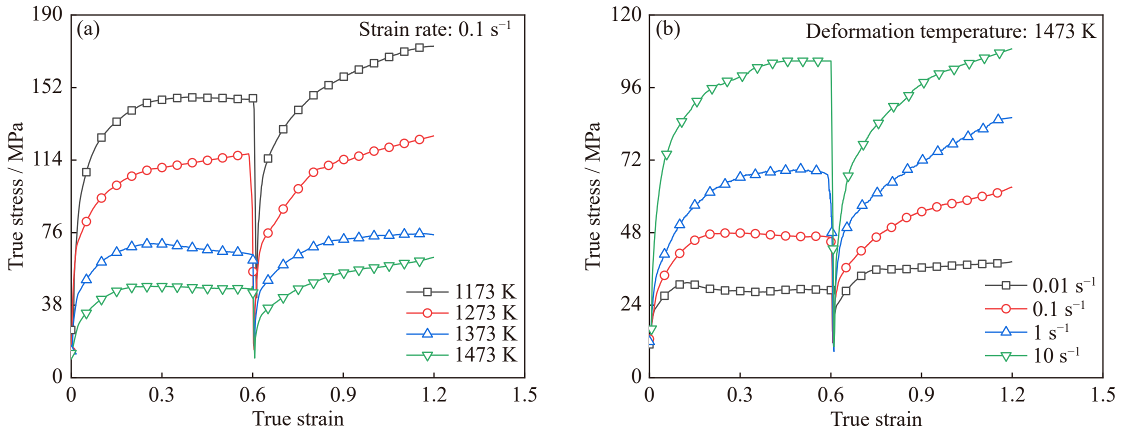

Fig. 3. Stress–strain curves at (a) different deformation temperatures and (b) different strain rates.

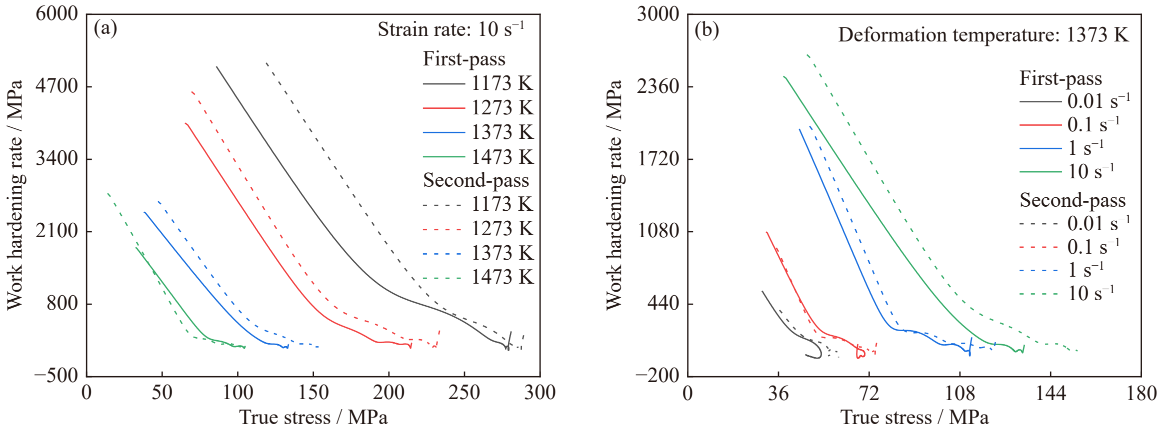

Fig. 4. Work hardening rates at (a) strain rate of 10 s^{-1} and (b) deformation temperature of 1373 K.

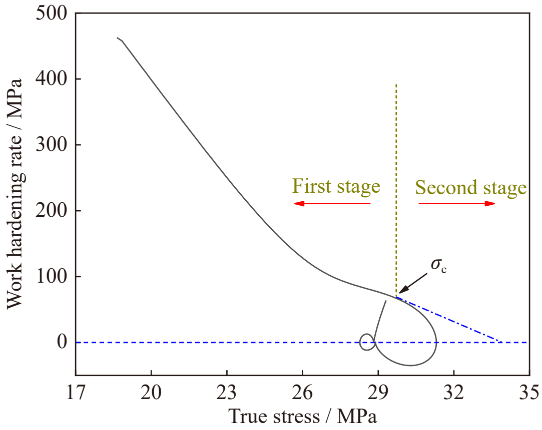

Fig. 5. Typical curve of work hardening rates during first-pass deformation at the deformation parameters of 1473 K and 0.01 s^{-1}.

ation process displays larger work hardening rates than the first-pass deformation. As the deformation temperature rises, the disparity in the work hardening rate of different deformation passes diminishes. It is generally known that deformation temperature has a close relationship with both the dynamic and static softening mechanisms. The dynamic softening process can effectively develop at high deformation temperatures, consuming the strain storage energy generated during the first-pass deformation. Furthermore, the static softening effect is also more significant at higher temperatures. As a result, the strain storage energy within the deformed material can be consumed adequately at high deformation temperatures before the second-pass deformation. The difference in the work hardening rate between various passes decreases as the strain rate goes down. At lower strain rates, the dynamic softening effect is more pronounced and can efficiently burn the strain storage energy generated during the first-pass deformation.

Generally, the representative curves of the work hardening rate can be separated into two or three stages. Fig. 5 displays the representative curves of work hardening rates consisting of two stages. In the first stage, the relationship between flow stress and work hardening rate is linear, and the work hardening rate reduces rapidly with the increasing flow stress. Because the dislocation annihilation and recombination occur at the initial deformation stage [33], this first stage starts when plastic deformation occurs and ends when DRX grains come into form. When the flow stress exceeds the value corresponding to the inflection point of work hardening rate curves, the second stage starts. Due to the impacts of DRX and dynamic recovery at this point, the work hardening rate falls to zero when flow stress hits the peak stress. After that, the flow stress keeps decreasing while the work hardening rate hardly changes. It suggests that work hardening and dynamic softening processes are in a dynamic equilibrium.

3.2. Constitutive modeling

3.2.1. Arrhenius constitutive model

According to Fig. 3, the difference in flow stress under various deformation passes is obvious. To characterize the impacts of deformation parameters and passes on flow behaviors, a trustworthy constitutive model must be established. In the study, the Arrhenius constitutive model is established to forecast the flow stress at various deformation conditions. The detailed form of the Arrhenius model is shown below [34–36]:

$$Z=\dot{\varepsilon}\exp\left(\frac{Q}{RT}\right)=\begin{cases}A_1\sigma^{n_1},(\alpha\sigma<0.8)\\ A_2\exp(\beta\sigma),(\alpha\sigma>1.2)\\ A[\sinh(\alpha\sigma)]^n,(\text{for all})\end{cases} \tag{2}$$

where Z is Zener-Hollomon parameter, $A_1, A_2, A, n_1, \beta, \alpha$, and n are material constants, R is gas constant, and Q is deformation activation energy. The flow stress at the strain of 0.1 is selected to calculate the above parameters in Eq. (2). The calculation process of those parameters in Eq. (2) is shown in Fig. 6.

Fig. 6 depicts the calculation process of those parameters at a specific strain. It is necessary to establish the link between these parameters and strain to forecast the flow stress at different deformation conditions accurately. These parameters n_1, β, n, Q, and A can be determined based on the calculation method shown in Fig. 6. Considering the various variation rules of parameters α, n, Q, and A at different deformation passes, it is necessary to establish a piecewise function for the flow behaviors of experimental LAHS steel. The detailed model is shown below:

$$\sigma=\frac{1}{\alpha}\sinh^{-1}\{\dot{\varepsilon}\exp[Q/(RT)]/A\}^{\frac{1}{n}} \tag{3}$$

During the first-pass deformation, these parameters in Arrhenius constitutive model can be expressed as below:

$$\begin{cases}\alpha=0.017-0.095\varepsilon+0.589\varepsilon^2-1.761\varepsilon^3+\\ \quad 2.512\varepsilon^4-1.371\varepsilon^5\\ n=5.149+9.562\varepsilon-97.582\varepsilon^2+304.348\varepsilon^3-\\ \quad 415.852\varepsilon^4+215.198\varepsilon^5\\ Q=(0.435-0.181\varepsilon+1.231\varepsilon^2-7.359\varepsilon^3+15.75\varepsilon^4-\\ \quad 10.727\varepsilon^5)\times10^6\\ \ln A=37.108-7.548\varepsilon+10.709\varepsilon^2-282.376\varepsilon^3+\\ \quad 809.076\varepsilon^4-612.109\varepsilon^5\end{cases} \tag{4}$$

During the second-pass deformation, these parameters in Arrhenius constitutive model can be expressed as below:

$$\begin{cases}\alpha=0.768-3.901\varepsilon+8.021\varepsilon^2-8.224\varepsilon^3+\\ \quad 4.198\varepsilon^4-0.853\varepsilon^5\\ n=(-2.8+15.292\varepsilon-32.382\varepsilon^2+33.861\varepsilon^3-\\ \quad 17.505\varepsilon^4+3.582\varepsilon^5)\times10^2\\ Q=(-1.031+5.747\varepsilon-11.978\varepsilon^2+12.218\varepsilon^3-\\ \quad 6.125\varepsilon^4+1.209\varepsilon^5)\times10^7\\ \ln A=(-1.095+6.069\varepsilon-12.712\varepsilon^2+13.055\varepsilon^3-\\ \quad 6.6\varepsilon^4+1.316\varepsilon^5)\times10^3\end{cases} \tag{5}$$

The comparison of the experimental and calculated flow stress at various deformation parameters is shown in Fig. 7. There is little variation between the experimental and calcu-

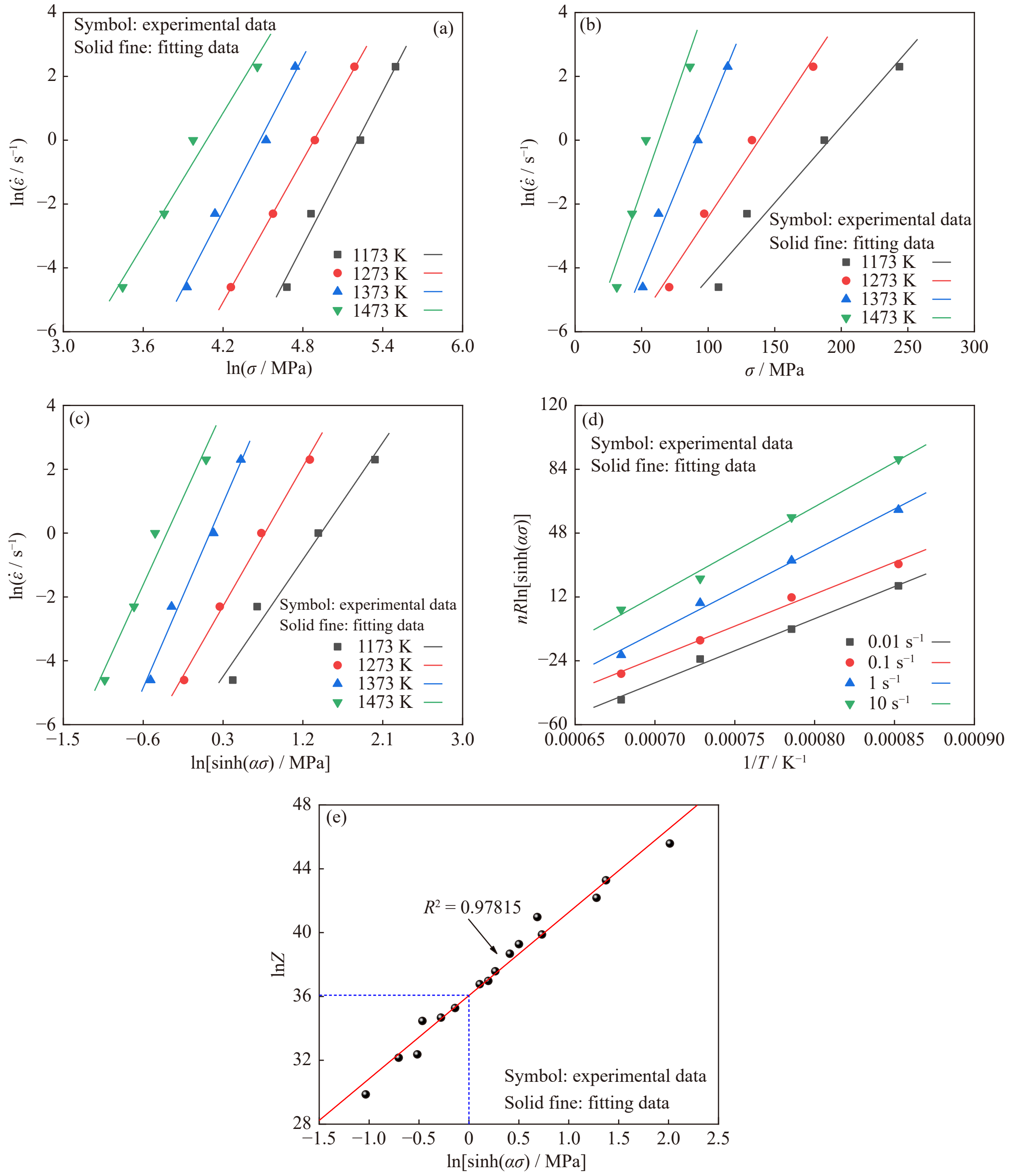

Fig. 6. Calculation process of (a) n_1, (b) β, (c) n, (d) Q, and (e) A.

lated flow stress of the first-pass deformation. However, at the second-pass deformation, there is a clear divergence between the experimental and calculated flow stress. It is ascribed to the coupling impacts of deformation parameters and deformation passes. It suggests that the Arrhenius model is not reliable to forecast the flow stress when the variation rule of flow stress is complex at various deformation conditions.

3.2.2. Modified Zerilli and Armstrong (ZA) model

Zerilli and Armstrong (ZA) constitutive model is semi-empirical, and it is widely used in many commercially finite element software [37]. Samantaray *et al.* [38] have modified the ZA model to forecast the flow stress of austenitic stainless steel during the single-pass deformation process. In the study, the modified ZA model is used to describe the flow behaviors of the experimental LAHS steel during the multi-pass deformation process. The detailed form of the modified ZA model is shown below:

$$\sigma = (B + B_1\varepsilon^{B_2})\exp[-(B_3 + B_4\varepsilon)T^* + (B_5 + B_6T^*)\ln\dot{\varepsilon}^*] \quad (6)$$

where B is the yield stress at the reference deformation temperature and strain rate, B_1–B_6 are material constants, $T^* = (T - T_{\text{ref}})$ with T_{ref} being the reference deformation temperature, and $\dot{\varepsilon}^* = \dot{\varepsilon}/\dot{\varepsilon}_{\text{ref}}$ with $\dot{\varepsilon}_{\text{ref}}$ being the reference strain rate. In the study, the reference deformation temperature and strain rate are determined to be 1473 K and 1 s^{-1}, respectively.

First, when T and $\dot{\varepsilon}$ are equal to T_{ref} and $\dot{\varepsilon}_{\text{ref}}$, Eq. (6) can be expressed as below:

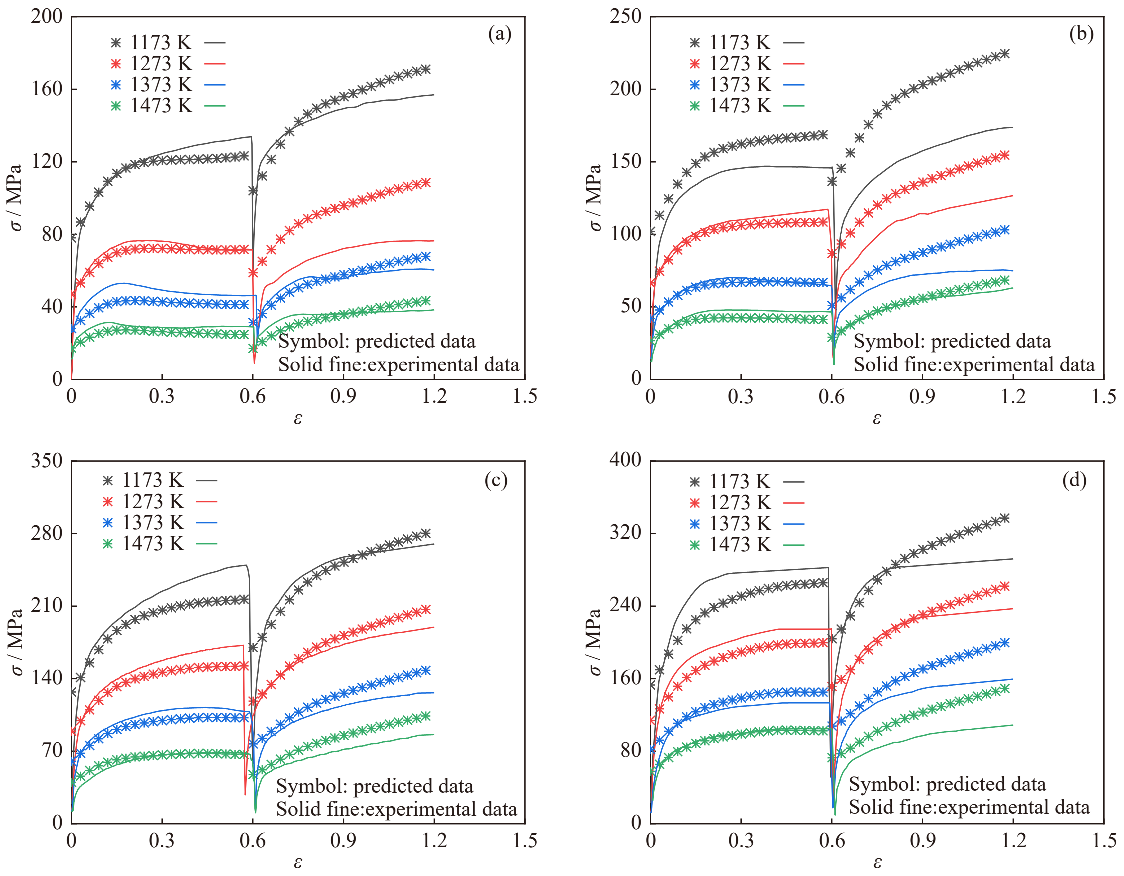

Fig. 7. Comparison of experimental and predicted flow stress at the strain rates of (a) 0.01, (b) 0.1, (c) 1, and (d) 10 s^{-1}.

$$\ln(\sigma - B) = \ln B_1 + B_2 \ln\varepsilon \tag{7}$$

As shown in Eq. (7), $\ln B_1$ and B_2 are the intercept and slope of the $\ln(\sigma - B)$ vs. $\ln\varepsilon$ plot, respectively.

Then, when $\dot{\varepsilon}$ is equal to $\dot{\varepsilon}_{\mathrm{ref}}$, Eq. (6) can be expressed as Eq. (8):

$$\ln\sigma = \ln(B + B_1\varepsilon^{B_2}) - (B_3 + B_4\varepsilon)T^* \tag{8}$$

According to Eq. (8), $-(B_3 + B_4\varepsilon)$ is the slope of $\ln\sigma$ vs. T^* plot, and the parameters B_3 and B_4 can calculated at various strains.

Finally, taking the natural logarithm of Eq. (6), Eq. (9) can be obtained as below:

$$\ln\sigma = \ln(B + B_1\varepsilon^{B_2}) - (B_3 + B_4\varepsilon)T^* + (B_5 + B_6T^*)\ln\dot{\varepsilon}^* \tag{9}$$

It is obvious that $(B_5 + B_6T^*)$ is the slope of $\ln\sigma$ vs. $\ln\dot{\varepsilon}^*$ plot, and parameters B_5 and B_6 can be calculated at different deformation temperatures.

These material constants in Eq. (6) can be obtained by Eqs. (7)–(9). These calculated results for the first-pass deformation and second-pass deformation are shown in Table 2. Fig. 8 shows the comparison of calculated and experimental flow stress at various deformation parameters. There is significant difference between the predicted and experimental flow stress. It indicates the modified ZA model is not suitable to establish the constitutive model for the experimental LAHS steel in the study.

Table 2. Values of the parameters in the modified ZA model

Deformation pass	B	B_1	B_2	B_3	B_4	B_5	B_6
First-pass	30.53	72.857	0.6626	0.0035	0.0017	0.1663	0.00014
Second-pass	31.88	43.926	1.9724	0.0057	−0.0016	0.1474	0.00007

3.2.3. Novel constitutive model

According to the discussions in Sections 3.2.1 and 3.2.2, the popular Arrhenius model and modified ZA model cannot forecast the flow stress of the experimental LAHS steel accurately. Moreover, the form of the Arrhenius model is complex, which is unfavorable to the application of the constitutive model in commercial software. To accurately forecast the flow stress, a novel and reliable constitutive model must be put out and constructed. Fields–Backofen (FB) model is a classical model for describing the flow stress, and its form is displayed below [39–40]:

$$\sigma = C\varepsilon^{C_1}\dot{\varepsilon}^{C_2} \tag{10}$$

where C, C_1, and C_2 are material constants. However, it cannot quantify the impacts of deformation temperature on flow stress. The FB model is modified by introducing the softening term, as shown in Eq. (11) [41]:

$$\sigma = D\varepsilon^{D_1}\dot{\varepsilon}^{D_2}(D_3T + D_4\varepsilon) \tag{11}$$

where D_1–D_4 are material constants. The relationship

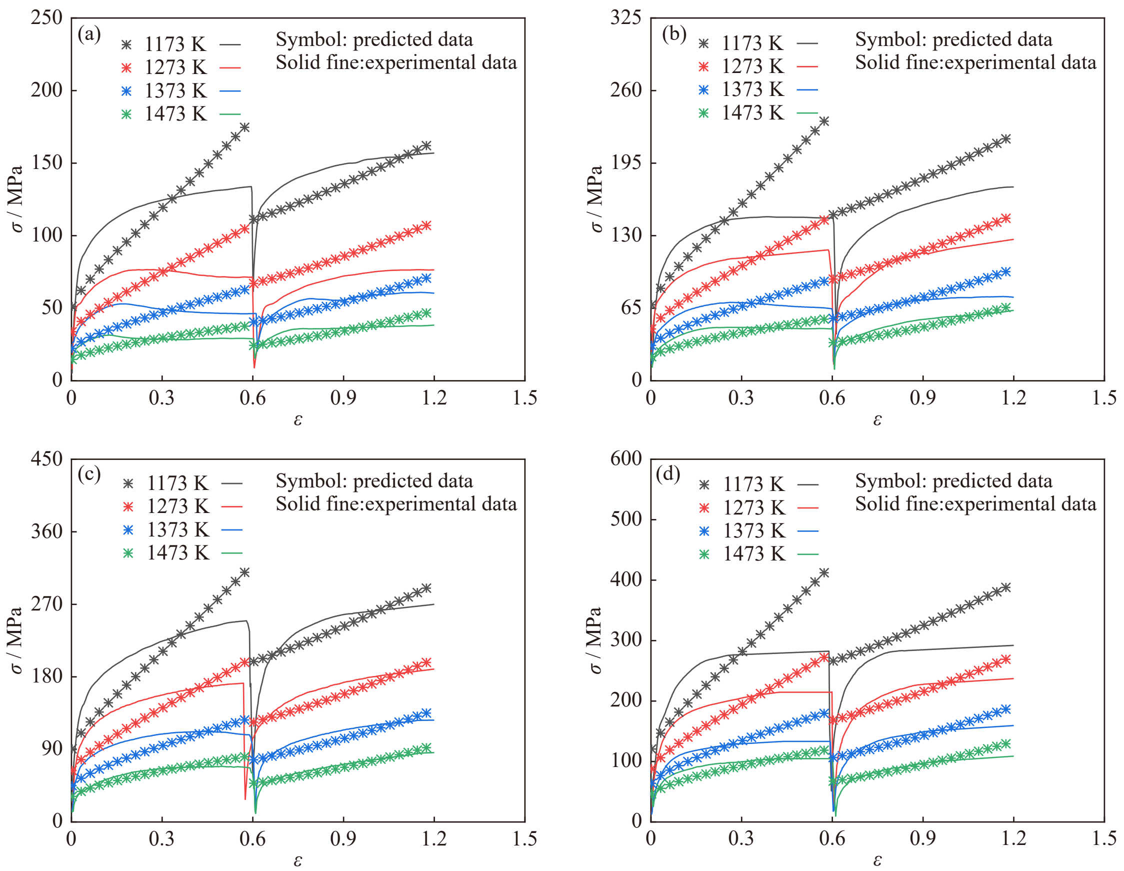

Fig. 8. Comparison of experimental and predicted flow stress at the strain rates of (a) 0.01, (b) 0.1, (c) 1, and (d) 10 s^{-1}.

between flow stress and deformation temperature is linear in Eq. (11). It is inconsistent with the variation rule of flow stress with deformation temperature in Fig. 3(a). Furthermore, the coupling effects of different deformation parameters have not been considered in Eq. (11). In the study, a new constitutive model is proposed as shown in Eq. (12):

$$\sigma = E\exp\left(\frac{E_1}{T}\right)\exp\left[(E_2 + E_3\dot{\varepsilon})\,\varepsilon\right]\varepsilon^{(E_4+E_5\dot{\varepsilon})}\dot{\varepsilon}^{(E_6+E_7\varepsilon)} \tag{12}$$

where E–E_7 are material constants. The effects of deformation temperature, strain rate, and strain on the flow characteristics are considered in Eq. (12). The relationship between the flow stress and the inverse of deformation temperature is an exponential function. Moreover, the completion of work hardening and dynamic softening can be reflected by the exponential and power functions of strain. Considering the strain rate sensitivity, the strain rate and strain are coupled in Eq. (12).

The method of multivariate nonlinear regression analysis can be used to calculate these material constants. Since the deformation process consists of multiple deformation passes, it is necessary to build the constitutive model in sections based on Eq. (12). The calculated parameters for various deformation passes are depicted in Table 3. Fig. 9 depicts a comparison of the experimental and calculated flow stress under various deformation parameters. The calculated results can match well with the experimental results. It suggests that the newly proposed model is trustworthy.

Table 3. Values of the parameters in the newly proposed model

Deformation pass	E	E_1	E_2	E_3	E_4	E_5	E_6	E_7
First-pass	1.202	6657.814	−0.525	−0.004	0.221	0.005	0.343	−244.672
Second-pass	5.368	6689.658	−1.813	−0.011	2.148	0.004	0.267	−149.862

3.2.4. Prediction accuracy analysis

The accuracy of the Arrhenius model and the newly proposed model is compared in this section. The mean absolute error (AARE), Pearson correlation coefficient (PCC), and relative error (RE) distribution are utilized to analyze the accuracy of these established models. The calculation method of AARE, PCC, and RE are shown below [42–44]:

$$\text{AARE} = \frac{1}{N}\sum_{i=1}^{N}\left|\frac{\sigma_{\text{e}i} - \sigma_{\text{p}i}}{\sigma_{\text{e}i}}\right| \times 100\% \tag{13}$$

$$\text{PCC} = \frac{\sum_{i=1}^{N}(\sigma_{\text{e}i} - \overline{\sigma}_{\text{e}})\left(\sigma_{\text{p}i} - \overline{\sigma}_{\text{p}}\right)}{\sqrt{\sum_{i=1}^{N}(\sigma_{\text{e}i} - \overline{\sigma}_{\text{e}})^2\sum_{i=1}^{N}\left(\sigma_{\text{p}i} - \overline{\sigma}_{\text{p}}\right)^2}} \tag{14}$$

$$\text{RE} = \left(\frac{\sigma_{\text{e}i} - \sigma_{\text{p}i}}{\sigma_{\text{e}i}}\right) \times 100\% \tag{15}$$

where $\sigma_{\text{e}i}$ and $\sigma_{\text{p}i}$ are the ith experimental and predicted flow stress, respectively, and $\overline{\sigma}_{\text{e}}$ and $\overline{\sigma}_{\text{p}}$ are the average values of experimental and predicted flow stress, respectively. According to Eqs. (13)–(15), Fig. 10 can be obtained. The

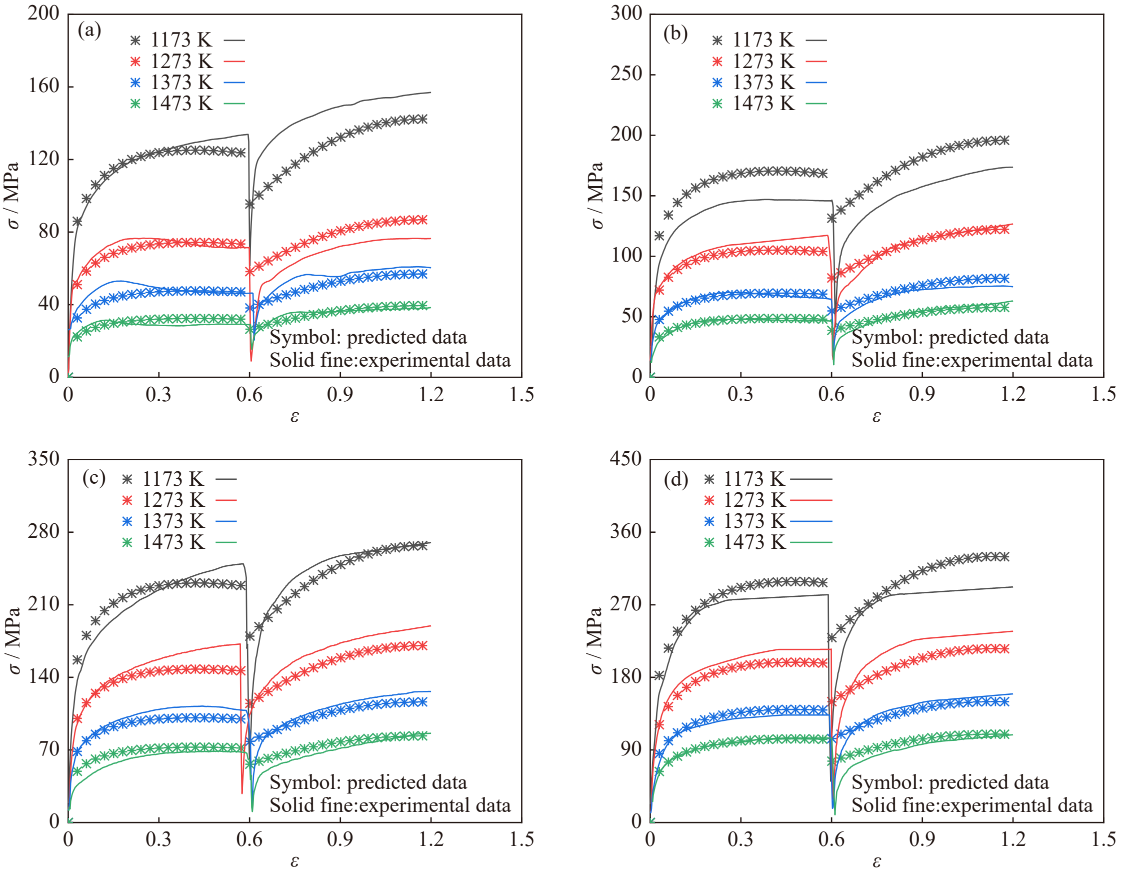

Fig. 9. Comparison of experimental and predicted flow stress at the strain rates of (a) 0.01, (b) 0.1, (c) 1, and (d) 10 s^{-1}.

PCC of Arrhenius constitutive model, modified ZA constitutive model, and the newly proposed constitutive model are 0.97412, 0.94847, and 0.98565, respectively. Moreover, the AARE of the newly proposed constitutive model is within 10%, which is lower than those of Arrhenius constitutive model and modified ZA constitutive model. According to Fig. 10(a), the max RE of the Arrhenius constitutive model exceeds 40%. It indicates the poor accuracy of the Arrhenius model. According to Fig. 10(b), the minimum RE of the modified ZA constitutive model exceeds −50%. According to Fig. 10(c), the RE of the new constitutive model is mainly between −10% and +10%. In conclusion, the newly proposed constitutive model can better forecast the variations of flow stress at various deformation parameters and deformation passes. Compared to the Arrhenius constitutive model and modified ZA constitutive model, the newly proposed constitutive model has higher prediction accuracy. Furthermore, the calculation process of those material parameters in the newly proposed constitutive model is simpler and more efficient.

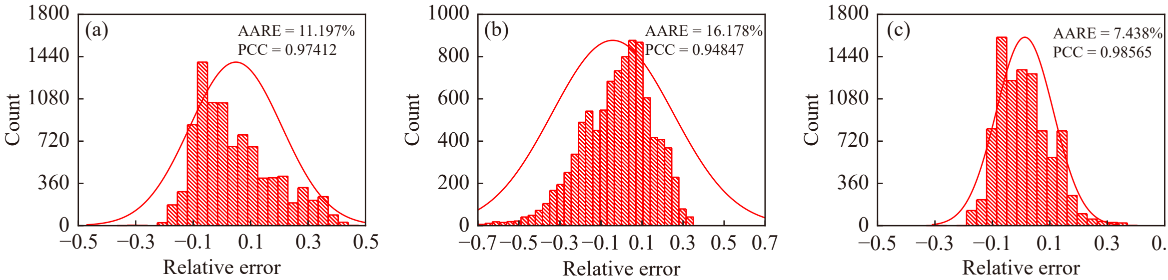

Fig. 10. Prediction accuracy of (a) Arrhenius model, (b) modified ZA model, and (c) newly proposed model.

3.3. Hot workability

3.3.1. Analysis of power dissipation efficiency

Power dissipation efficiency (PDE, μ) is a parameter that can evaluate the efficiency of dissipating energy by microstructure evolution. It can be calculated by Eq. (16) [45–46]:

$$\mu = \frac{2m}{m+1} \tag{16}$$

where m is strain rate sensitivity factor, and its calculation method is shown below [47–48]:

$$m = \frac{\partial \ln\sigma}{\partial \ln\dot{\varepsilon}} \tag{17}$$

According to Eqs. (16) and (17), the variation of PDE depends on the strain rate, strain, and deformation temperature. Therefore, the impacts of different deformation parameters on PDE were analyzed, as shown in Fig. 11. Fig. 11(a) displays the variation of PDE at 1473 K. The PDE rises with the increasing strain and decreasing strain rate during the first-pass deformation, because there is ample time for DRX development at a low strain rate and more strain storage energy for DRX development at large strain. During the second-pass deformation, the variation rule of PDE is complex. The PDE grows with increasing strain rate at the beginning period of second-pass deformation. As the deformation process continues, the PDE keeps constant at different strain rates. When the strain exceeds 0.82, the PDE reduces as the strain rate increases. Furthermore, when the strain increases, the PDE rises at low strain rates and decreases at high strain rates.

The microstructures corresponding to the regions R1 and R2 are selected to explore the causes of abnormal change in PDE during second-pass deformation, as displayed in Fig. 12. According to Fig. 12(a), the microstructure is composed of coarse and equiaxed grains with straight grain boundaries at the deformation parameters of 1473 K and 10 s^{-1}. It indicates that the DRX can develop adequately, and the grain growth occurs during the second-pass deformation. At these deformation conditions, the DRX cannot develop adequately during the first-pass deformation due to the short deformation time. So, the peak PDE is 29.4% during the first-pass deformation, and it is not very high. There is much strain storage energy within the experimental LAHS steel. During the inter-pass soaking process, the metadynamic recrystallization can develop sufficiently driven by the strain storage en-

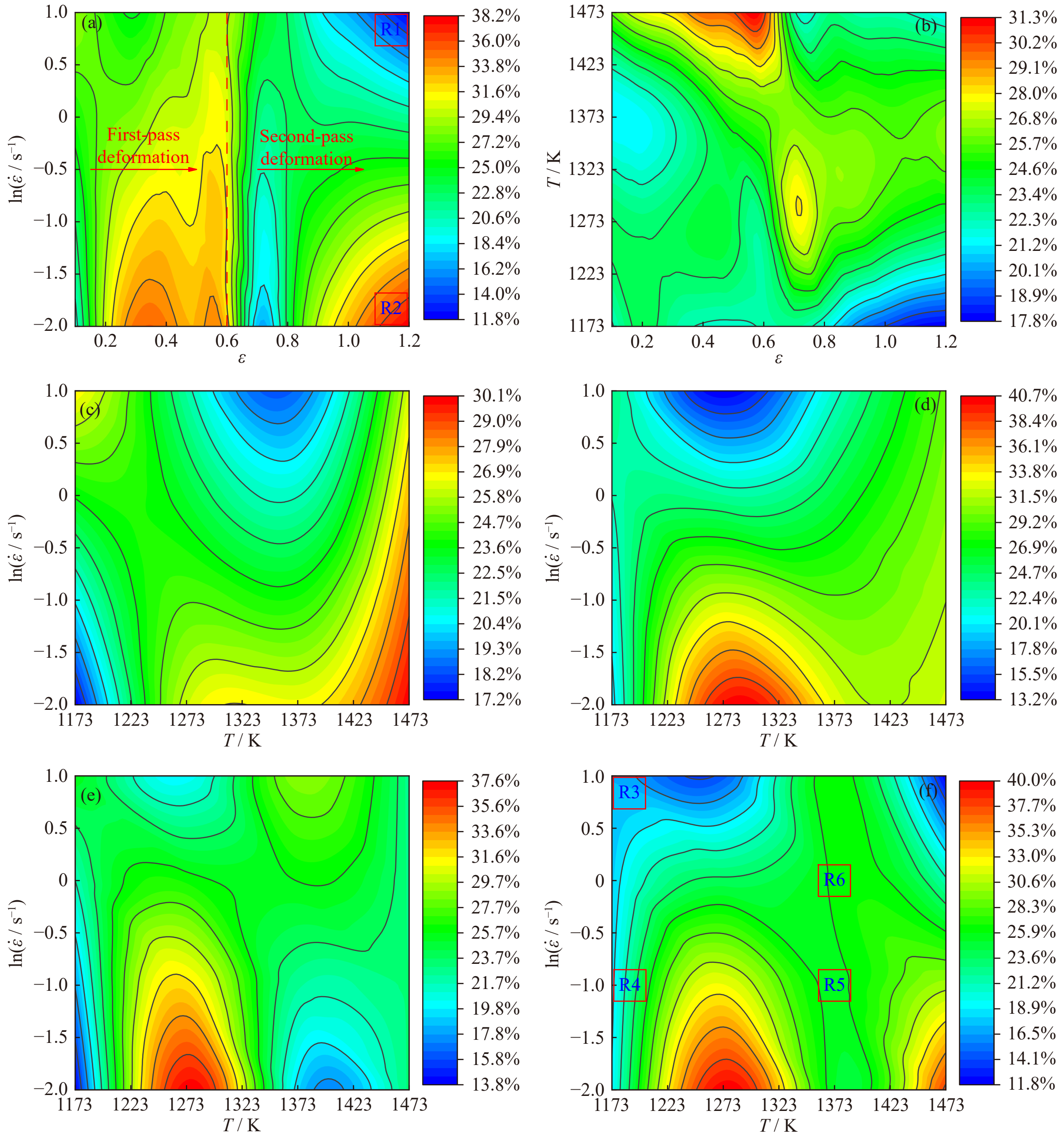

Fig. 11. PDE maps at (a) deformation temperature of 1473 K, (b) strain rate of 1 s^{-1}, (c) strain of 0.2, (d) strain of 0.6, (e) strain of 0.8, and (f) strain of 1.2.

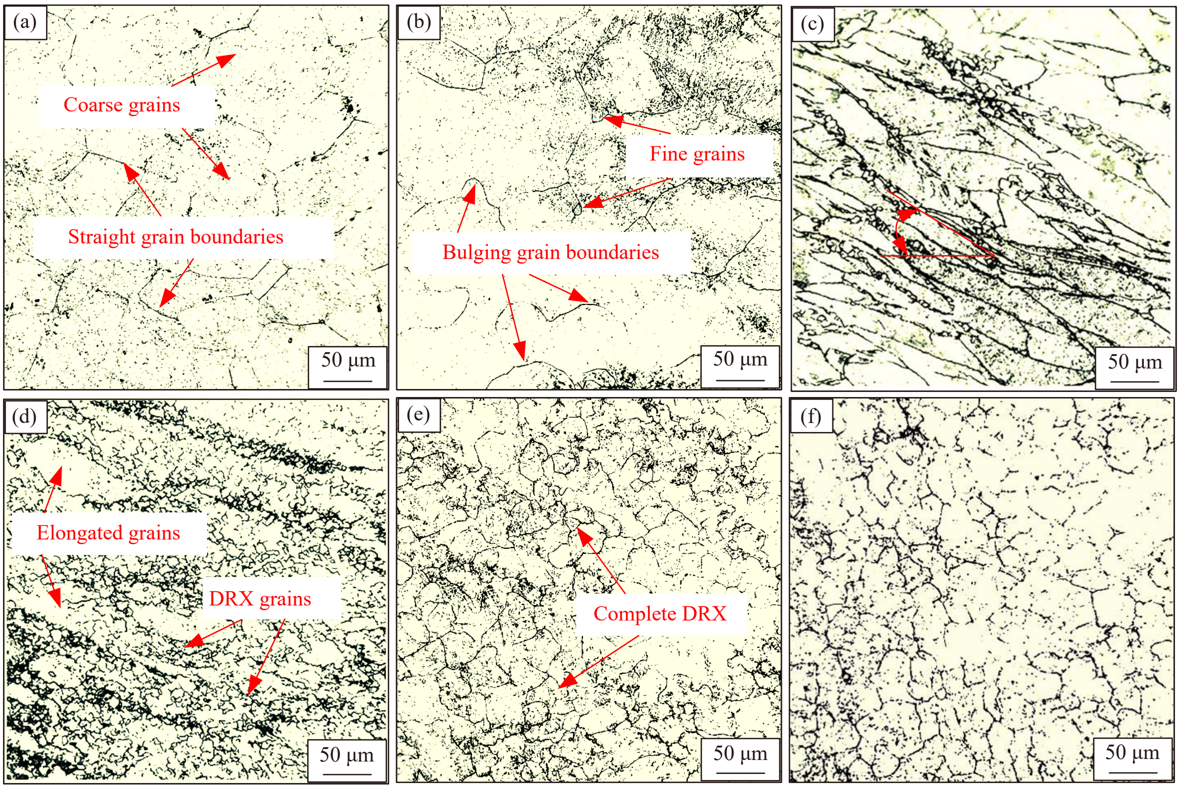

Fig. 12. Microstructures corresponding to regions (a) R1, (b) R2, (c) R3, (d) R4, (e) R5, and (f) R6 in Fig. 11.

ergy, and the grains are refined [12,49]. During the second-pass deformation, the fine grains can promote DRX development, and the PDE is large at the initial stage of second-pass deformation [50–51]. Adequate DRX development and grain growth occur at larger strains. As a result, the PDE decreases at larger strain during second-pass deformation. Fig. 12(b) displays the microstructure at the deformation parameters of 1473 K and 0.01 s^{-1}. The grains are coarse, and the grain boundaries appear serrated. Besides, there are a few fine grains inside the material. It suggests that secondary DRX occurs at these deformation conditions. When the strain rate is low and the deformation temperature is high, the adequate DRX process occurs during the first-pass deformation due to the sufficient deformation time and high deformation temperature, and the PDE is high during the first-pass deformation. DRX grains grow up at high temperatures during the inter-pass soaking process, which is adverse for DRX development in the subsequent deformation process. As a result, the PDE is very low at the initial period of second-pass deformation, which means difficulty in DRX development. The strain storage energy increases with the increasing strain, which can promote the development of secondary DRX. So, the PDE increases as the strain rises during second-pass deformation. It can be concluded that the abnormal variations in PDE with the strain and strain rate are attributed to the DRX development.

Fig. 11(b) shows the variation of PDE at the strain rate of 1 s^{-1}. During the first-pass deformation, the peak PDE occurs at 1473 K. During the second-pass deformation, the peak PDE corresponds to 1273 K. Because grain growth occurs at higher deformation temperature, it is difficult for the DRX development at lower deformation temperature. Fig. 11(c)–(f) displays the variations of PDE at different deformation temperatures and strain rates. It is the first-pass deformation when the strain is below 0.6. The deformation parameters corresponding to peak PDE shift from high deformation temperature and low strain rate to low deformation temperature and low strain rate with increasing strain. Because the peak PDE corresponds to the deformation situation with the most intense DRX process. At a strain of 0.8, the peak PDE corresponds to the deformation parameters of 1226–1323 K and 0.01–0.21 s^{-1}, and the PDE is below 23.7% at higher deformation temperatures. At strain of 1.2, the peak PDE values correspond to deformation parameters of 1213–1340 K and 0.01–0.17 s^{-1} and 1435–1473 K and 0.01–0.09 s^{-1}. According to Fig. 12(b), there are both coarse and fine grains inside the experimental LAHS steel at the deformation parameters of 1435–1473 K and 0.01–0.09 s^{-1}. It is harmful to the mechanical properties. According to the above discussions, the PDE can be used to evaluate the DRX process well. However, the peak PDE does not always correspond to the optimal deformation parameters interval during the multi-pass deformation process. The PDE can only reflect the DRX development at a specific strain, and cannot be used to evaluate the overall DXR development during the deformation process. Therefore, the variation in grain size should be considered when optimizing processing parameters.

In order to better study the relationship between PDE and microstructures, regions R3–R6 in Fig. 11(f) are chosen to analyze the microstructures, as displayed in Fig. 12(c)–(f). Region R3 corresponds to the deformation parameters of 1173 K and 10 s^{-1}. At this deformation condition, the PDE is

17.26%. It suggests that there is little energy for the microstructure evolution. According to Fig. 12(c), there are many elongated grains and a few DRX grains, which is consistent with PDE. Furthermore, elongated grains are in a certain direction, indicating that plastic instability is easy to occur [52]. Region R4 corresponds to the deformation parameters of 1173 K and 0.1 s^{-1}, and the PDE is 18.43%. According to Fig. 12(d), the DRX process is incomplete, but the DRX degree exceeds that of region R3. Region R5 corresponds to the deformation parameters of 1373 K and 0.1 s^{-1}, where the PDE is 25.64%. It is much higher than that of regions R3 and R4. According to Fig. 12(e), complete DRX and grain growth occur. Region R6 corresponds to the deformation parameters of 1373 K and 1 s^{-1}. At this deformation condition, the PDE is 26.12%. Also, complete DRX occurs at the deformation condition.

3.3.2. Analysis of instability factor

In addition to PDE, the instability factor (IF) is also a valid indicator to study the workability of materials. According to the reported literature, IF can be calculated by Eq. (18) [53–54]:

$$\xi = \frac{\partial \ln[m/(m+1)]}{\partial \ln \dot{\varepsilon}} + m \tag{18}$$

where ξ is IF. When the IF is below zero, flow instability may occur.

According to Eq. (18), the IF at various deformation parameters can be calculated, as depicted in Fig. (13). Fig. 13(a) displays the variations of IF at the strains of 0.2–0.6. There is no instability region at the strain of 0.2. As the strain increases, the flow instability occurs at high strain rates. Compared to the IF at the strain of 0.4, the IF at the strain of 0.6 is smaller. It means that the more dramatic flow instability occurs at larger strain. Fig. 13(b) shows the variation of IF at the strains of 0.8–1.2. The variation rule of IF with strain during the second-pass deformation is similar to that during the first-pass deformation. At the strain of 1.2, the deformation parameters corresponding to instability regions are 1182–1320 K and 0.28–10 s^{-1} and 1448–1473 K and 0.25–10 s^{-1}.

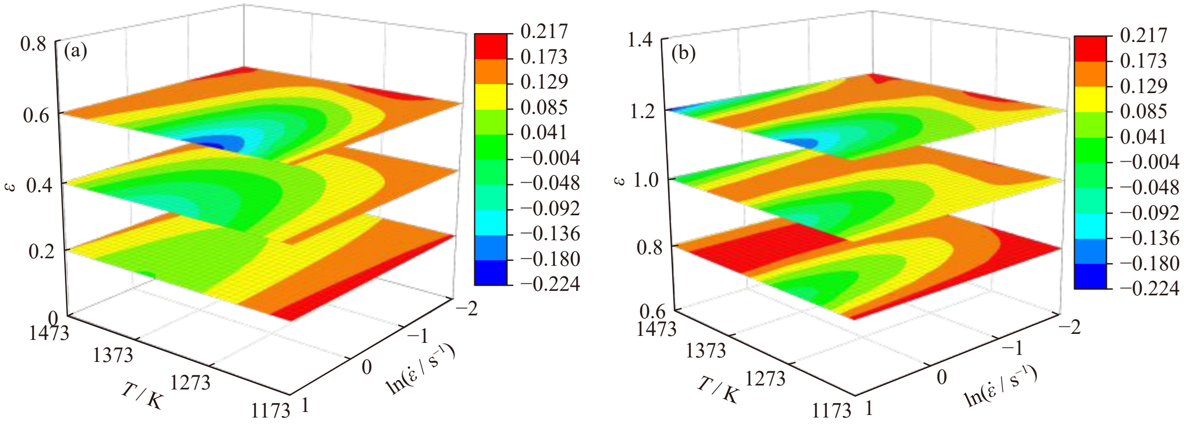

Fig. 13. IF at (a) strains of 0.2–0.6 and (b) strains of 0.8–1.2.

3.3.3. Integrated processing maps

According to the above discussions, the PDE can be utilized to evaluate DRX development at a specific strain. However, when multiple DRX occur within the material, the PDE cannot optimize the processing parameters well. For example, the coarse grains may occur at these deformation parameters corresponding to peak PDE in Fig. 11(a). It means that the peak PDE cannot be used to evaluate the hot workability of the LAHS steel during the multi-pass deformation process. In the study, the variations in grain size and distribution are considered when optimizing the processing parameters. The average size of DXR grains and overall grains within the experimental LAHS steel is counted. As a result, a new method for the optimization of processing parameters is proposed, and the hot workability can be evaluated well by an integrated processing map, which considers the effects of PDE, IF, and distribution and size of grains.

The integrated processing map is displayed in Fig. 14. The black contour lines represent the average size of DRX grains. The colored contours represent the average size of overall grains. The white contour lines represent PDE, and the grid lines represent IF. When optimizing processing parameters, the deformation parameters relevant to unstable zones should be excluded. According to Fig. 14, there is no intersection between the interval of deformation parameters corresponding to peak PDE and IF. As a result, the optimizing processing parameters are deformation parameters of 1213–1340 K and 0.01–0.17 s^{-1} and 1435–1473 K and 0.01–0.09 s^{-1}. However, according to the average size of overall grains and DRX grains, these grains in the experimental LAHS steel are coarse under the deformation parameters of 1435–1473 K and 0.01–0.09 s^{-1}. For the forming of heavy components, coarse grains should be voided. As is well known, grain refinement is one important way to improve the strength and ductility of alloys [55–57]. At the deformation parameter of 1213–1340 K and 0.01–0.17 s^{-1}, there are partial regions corresponding to deformation parameters that the average size of DRX grains and overall grains are not equal, which suggests that there is incomplete DRX within the material. Besides, the requirement of grain size number is 6–8 grade for the forgings. As a result, the optimized deformation parameters are 1223–1318 K and 0.01–0.08 s^{-1}. The average grain size is 18.36–42.3 μm within the optimized processing parameters. According to the above analysis, the integrated processing map can optimize the processing parameters well. Compared to the traditional processing map, the integrated processing map can be used to optimize the processing map with more accurate intervals. Furthermore, it can ensure that the DRX process develops adequately, no flow instability occurs, and grain size is uniform and fine.

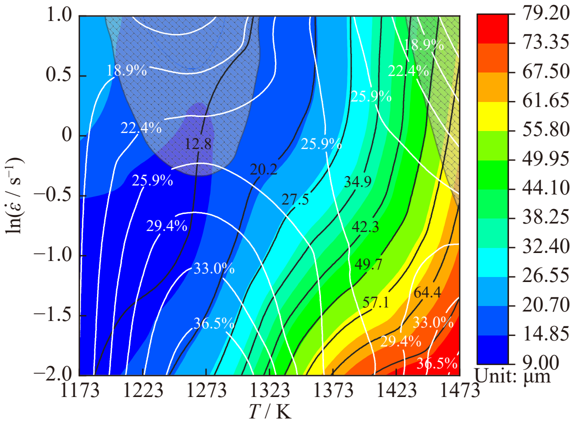

Fig. 14. Integrated processing maps of experimental LAHS steel under multi-pass deformation.

4. Conclusions

In the study, the deformation behaviors of the experimental LAHS steel are studied. The main conclusions are shown below:

(1) The work hardening rate increases with the decreasing deformation temperature and increasing strain rate during the multi-pass deformation process. The work hardening rate of the second-pass deformation is greater than that of the first-pass deformation.

(2) A novel constitutive model, considering the coupling impacts of deformation parameters, is proposed to forecast the flow stress of experimental LAHS steel during the multi-pass deformation process. The newly proposed model shows higher accuracy than that of Arrhenius model with a PCC of 0.98565.

(3) An integrated processing map is proposed to study the hot workability of experimental LAHS steel during the multi-pass deformation process, which considers the effects of PDE, IF, and distribution and size of grains.

(4) The optimized deformation parameters are 1223–1318 K and 0.01–0.08 s^{-1}. The average size of DRX grains and overall grains is 18.36–42.3 μm within the optimized processing parameters, which can meet the requirement of grain size number of 6–8 grade for the heavy forgings.

Acknowledgements

This work was financially supported by National Natural Science Foundation of China (No. 52305373), Jiangxi Provincial Natural Science Foundation (No. 20232BAB214053), Science and Technology Major Project of Jiangxi, China (No. 20194ABC28001), Fund of Jiangxi Key Laboratory of Forming and Joining Technology for Aerospace Components, Nanchang Hangkong University (No. EL202303299), and PhD Starting Foundation of Nanchang Hangkong University (No, EA202303235).

Conflict of Interest

The authors declare that there is no conflict of interest.

References

[1] M.J. Zhao, L. Huang, C.M. Li, J.J. Li, and P.C. Li, Evaluation of the deformation behaviors and hot workability of a high-strength low-alloy steel, *Mater. Sci. Eng. A*, 810(2021), art. No. 141031.

[2] R.C. Chen, S.Y. Zhang, M. Wang, X.L. Liu, and F. Feng, Unified modelling of flow stress and microstructural evolution of 300M steel under isothermal tension, *Metals*, 11(2021), No. 7, art. No. 1086.

[3] J.J. Qiu, M. Zhang, X.Y. Liu, X.X. Zhang, and Z.L. Tan, Characterization of retained austenite in a low carbon high strength Mn–Si–Cr steel, *Mater. Sci. Eng. A*, 797(2020), art. No. 139985.

[4] S.B. Qiao, X.K. He, C.S. Xie, and Z.D. Liu, Static recrystallization behavior of SA508Gr.4N reactor pressure vessel steel during hot compressive deformation, *J. Iron Steel Res. Int.*, 28(2021), No. 5, p. 604.

[5] M.J. Zhao, L. Huang, R. Zeng, D.X. Wen, H.L. Su, and J.J. Li, *In-situ* observations and modeling of static recrystallization in 300 M steel, *Mater. Sci. Eng. A*, 765(2019), art. No. 138300.

[6] B. Fang, G.F. Tian, Z. Ji, M.Y. Wang, C.C. Jia, and S.W. Yang, Study on the thermal deformation behavior and microstructure of FGH96 heat extrusion alloy during two-pass hot deformation, *Int. J. Miner. Metall. Mater.*, 26(2019), No. 5, p. 657.

[7] B. Fang, Z. Ji, M. Liu, *et al.*, Study on constitutive relationships and processing maps for FGH96 alloy during two-pass hot deformation, *Mater. Sci. Eng. A*, 590(2014), p. 255.

[8] Y. Cheng, H.Y. Du, Y.H. Wei, L.F. Hou, and B.S. Liu, Metadynamic recrystallization behavior and workability characteristics of HR3C austenitic heat-resistant stainless steel with processing map, *J. Mater. Process. Technol.*, 235(2016), p. 134.

[9] S. Ding, T. Taylor, S.A. Khan, Y. Sato, and J. Yanagimoto, Further understanding of metadynamic recrystallization through thermomechanical tests and EBSD characterization, *J. Mater. Process. Technol.*, 299(2022), art. No. 117359.

[10] R. Zeng, L. Huang, J.J. Li, H.W. Li, H. Zhu, and X.T. Zhang, Quantification of multiple softening processes occurring during multi-stage thermoforming of high-strength steel, *Int. J. Plast.*, 120(2019), p. 64.

[11] N. Bayat, G.R. Ebrahimi, A. Momeni, and H.R. Ezatpour, Microstructural evolution of a superaustenitic stainless steel during a two-step deformation process, *Int. J. Miner. Metall. Mater.*, 25(2018), No. 2, p. 181.

[12] Q.W. Wang, Y.C. Lin, Y.Q. Jiang, *et al.*, Precipitation behavior of a β-quenched Ti–5Al–5Mo–5V–1Cr–1Fe alloy during high-temperature compression, *Mater. Charact.*, 151(2019), p. 358.

[13] Y.C. Lin, F. Wu, Q.W. Wang, D.D. Chen, and S.K. Singh, Microstructural evolution of a Ni–Fe–Cr-base superalloy during non-isothermal two-stage hot deformation, *Vacuum*, 151(2018), p. 283.

[14] S. Ding, J.W. Zhang, S.A. Khan, and J. Yanagimoto, Static recovery of A5083 aluminum alloy after a small deformation through various measuring approaches, *J. Mater. Sci. Technol.*, 104(2022), p. 202.

[15] Y. Xu, Y.X. Jiao, and J.S. Liu, Modeling of metadynamic recrystallization kinetics and recrystallization mechanisms of V-containing 12Cr rotor steel, *J. Mater. Eng. Perform.*, 29(2020), No. 7, p. 4754.

[16] H.J. Liu, Q. Wang, J.S. Zhang, K.H. Xu, and Y. Xue, Effect of multi-pass deformation on hot flow behavior and microstructure evolution mechanism of Ti–6Al–4V alloy fabricated by hot isostatic pressing, *J. Mater. Res. Technol.*, 17(2022), p. 2229.

[17] Q. Ma, K. Wei, Y. Xu, L.J. Zhao, and X. Zhang, Exploration of the static softening behavior and dislocation density evolution of TA15 titanium alloy during double-pass hot compression deformation, *J. Mater. Res. Technol.*, 18(2022), p. 872.

[18] J. Tang, F.L. Jiang, C.H. Luo, *et al*., Integrated physically based modeling for the multiple static softening mechanisms following multi-stage hot deformation in Al–Zn–Mg–Cu alloys, *Int. J. Plast.*, 134(2020), art. No. 102809.

[19] B. Jia, H.R. Ma, and Y. Peng, A dislocation density-based unified constitutive model of multipass deformation, *Steel Res. Int.*, 91(2020), No. 2, art. No. 1900372.

[20] J. Wang, G. Chen, S.H. Huang, *et al*., Multi-scale modeling and simulation for multi-pass processing of Ta–2.5 W alloy, *Int. J. Mech. Sci.*, 218(2022), art. No. 107069.

[21] X. Nie, S. Dong, F.H. Wang, *et al*., Flow behavior and formability of hot-rolled Mg–8Gd–3Y alloy under double-pass isothermal compression, *J. Mater. Process. Technol.*, 275(2020), art. No. 116328.

[22] T.K. Sakai, A. Belyakov, R. Kaibyshev, H. Miura, and J.J. Jonas, Dynamic and post-dynamic recrystallization under hot, cold and severe plastic deformation conditions, *Prog. Mater. Sci.*, 60(2014), p. 130.

[23] R. Zeng, L. Huang, H.L. Su, H.J. Ma, Y.F. Ma, and J.J. Li, Softening characterization of 300M high-strength steel during post-dynamic recrystallization, *Metals*, 8(2018), No. 5, art. No. 340.

[24] C.M. Li, L. Huang, M.J. Zhao, X.T. Zhang, J.J. Li, and P.C. Li, Influence of hot deformation on dynamic recrystallization behavior of 300M steel: Rules and modeling, *Mater. Sci. Eng. A*, 797(2020), art. No. 139925.

[25] Y.B. Xiong, D.X. Wen, Z.Z. Zheng, C.Y. Sun, J. Xie, and J.J. Li, Comparative study of wire arc additive manufactured and wrought ultrahigh-strength steels: Flow behavior and microstructure evolution, *Met. Mater. Int.*, 29(2023), No. 10, p. 3009.

[26] H. Wang, D. Liu, J.G. Wang, H.P. Wang, Y. Hu, and H.D. Rao, Characterization of hot deformation behavior of 30Si2MnCrMoVE low-alloying ultra-high-strength steel by constitutive equations and processing maps, *J. Iron Steel Res. Int.*, 27(2020), No. 7, p. 807.

[27] M.J. Zhao, L. Huang, R. Zeng, H.L. Su, D.X. Wen, and J.J. Li, *In-situ* observations and modeling of metadynamic recrystallization in 300M steel, *Mater. Charact.*, 159(2020), art. No. 109997.

[28] R.C. Chen, J. Zeng, G.C. Yao, and F. Feng, Flow-stress model of 300M steel for multi-pass compression, *Metals*, 10(2020), No. 4, art. No. 438.

[29] M.J. Zhao, L. Huang, C.M. Li, *et al*., Flow stress characteristics and constitutive modeling of typical ultrahigh-strength steel under high temperature and large strain, *Steel Res. Int.*, 94(2023), No. 3, art. No. 2200648.

[30] M.J. Zhao, L. Huang, C.M. Li, *et al*., Investigation and modeling of austenite grain evolution for a typical high-strength low-alloy steel during soaking and deformation process, *Acta Metall. Sin.*, 35(2022), No. 6, p. 996.

[31] K. Kishore, R.G. Kumar, and A.K. Chandan, Critical assessment of the strain-rate dependent work hardening behaviour of AISI 304 stainless steel, *Mater. Sci. Eng. A*, 803(2021), art. No. 140675.

[32] K.K. Kumar, A. Kumar, and S. Sundar, Investigation of microstructure characteristics and work hardening behaviour of water-cooled FSW dissimilar aluminium alloys, *Mater. Today Commun.*, 35(2023), art. No. 105857.

[33] D.X. Wen, Y.C. Lin, J. Chen, *et al*., Work-hardening behaviors of typical solution-treated and aged Ni-based superalloys during hot deformation, *J. Alloys Compd.*, 618(2015), p. 372.

[34] Y.S. Li, Y.W. Dong, Z.H. Jiang, Q.F. Tang, S.Y. Du, and Z.W. Hou, Influence of rare earth Ce on hot deformation behavior of as-cast Mn18Cr18N high nitrogen austenitic stainless steel, *Int. J. Miner. Metall. Mater.*, 30(2023), No. 2, p. 324.

[35] J.C. Long, Q.X. Xia, G.F. Xiao, Y. Qin, and S. Yuan, Flow characterization of magnesium alloy ZK61 during hot deformation with improved constitutive equations and using activation energy maps, *Int. J. Mech. Sci.*, 191(2021), art. No. 106069.

[36] J. Wang, F. Zhao, G.L. Xie, J.X. Xu, and X.H. Liu, Hot compressive deformation of eutectic Al–17at% Cu alloy on the interface of the Cu–Al composite plate produced by horizontal continuous casting, *Int. J. Miner. Metall. Mater.*, 29(2022), No. 8, p. 1578.

[37] Y. Liu, M. Li, X.W. Ren, Z.B. Xiao, X.Y. Zhang, and Y.C. Huang, Flow stress prediction of Hastelloy C-276 alloy using modified Zerilli–Armstrong, Johnson–Cook and Arrhenius-type constitutive models, *Trans. Nonferrous Met. Soc. China*, 30(2020), No. 11, p. 3031.

[38] D. Samantaray, S. Mandal, U. Borah, A.K. Bhaduri, and P.V. Sivaprasad, A thermo-viscoplastic constitutive model to predict elevated-temperature flow behaviour in a titanium-modified austenitic stainless steel, *Mater. Sci. Eng. A*, 526(2009), No. 1-2, p. 1.

[39] Y.L. Lin, K. Zhang, Z.B. He, X.B. Fan, Y.D. Yan, and S.J. Yuan, Constitutive modeling of the high-temperature flow behavior of α-Ti alloy tube, *J. Mater. Eng. Perform.*, 27(2018), No. 5, p. 2475.

[40] Y.C. Lin and X.M. Chen, A critical review of experimental results and constitutive descriptions for metals and alloys in hot working, *Mater. Des.*, 32(2011), No. 4, p. 1733.

[41] N. Kotkunde, H. Nitin Krishnamurthy, A. Kumar Gupta, and S. Kumar Singh, Study of hot deformation behavior using phenomenological based constitutive model for austenitic stainless steel 316, *Mater. Today Proc.*, 5(2018), No. 2, p. 4870.

[42] A. Mohamadizadeh, A. Zarei-Hanzaki, and H.R. Abedi, Modified constitutive analysis and activation energy evolution of a low-density steel considering the effects of deformation parameters, *Mech. Mater.*, 95(2016), p. 60.

[43] A. Shamsolhodaei, A. Zarei-Hanzaki, M. Ghambari, and S. Moemeni, The high temperature flow behavior modeling of NiTi shape memory alloy employing phenomenological and physical based constitutive models: A comparative study, *Intermetallics*, 53(2014), p. 140.

[44] Z.Y. Ding, Q.D. Hu, L. Zeng, and J.G. Li, Hot deformation characteristics of as-cast high-Cr ultra-super-critical rotor steel with columnar grains, *Int. J. Miner. Metall. Mater.*, 23(2016), No. 11, p. 1275.

[45] Y. Xue, S.S. Chen, Z.M. Zhang, Q. Wang, and J.P. Yan, Hot workability and microstructure evolution of Al–0.2Sc–0.04Zr alloy, *J. Mater. Sci.*, 54(2019), No. 10, p. 7908.

[46] Q. Chen, L. Hu, M.G. Li, *et al*., Optimizing process parameters of as-homogenized Mg–Gd–Y–Zn–Zr alloy in isothermal uniaxial compression on the basis of processing maps via prasad criterion and murty criterion, *J. Mater. Eng. Perform.*, 31(2022), No. 3, p. 2257.

[47] M.S. Ghazani and B. Eghbali, Strain hardening behavior, strain rate sensitivity and hot deformation maps of AISI 321 austenitic stainless steel, *Int. J. Miner. Metall. Mater.*, 28(2021), No. 11, p. 1799.

[48] C.M. Li, L. Huang, M.J. Zhao, S.Q. Guo, and J.J. Li, Study on microstructure evolution and deformation mechanism of Ti-

6554 based on power dissipation efficiency at supertransus temperatures, *J. Alloys Compd.*, 924(2022), art. No. 166481.

[49] A. Paggi, G. Angella, and R. Donnini, Strain induced grain boundary migration effects on grain growth of an austenitic stainless steel during static and metadynamic recrystallization, *Mater. Charact.*, 107(2015), p. 174.

[50] R.Q. Lu, Z.M. Xu, F.L. Jiang, *et al.*, Revealing the grain size dependent hot workability and deformation mechanisms in a Mg–Zn–Y alloy, *J. Magnes. Alloys*, 11(2023), No. 4, p. 1461.

[51] G.Q. Chen, G.S. Fu, T.Y. Wei, C.Z. Cheng, H.S. Wang, and J.D. Wang, Effect of initial grain size on the dynamic recrystallization of hot deformation for 3003 aluminum alloy, *Met. Mater. Int.*, 24(2018), No. 4, p. 711.

[52] X.F. Ding, F.Q. Zhao, Y.H. Shuang, L.F. Ma, Z.B. Chu, and C.J. Zhao, Characterization of hot deformation behavior of as-extruded AZ31 alloy through kinetic analysis and processing maps, *J. Mater. Process. Technol.*, 276(2020), art. No. 116325.

[53] H.T. Lu, D.Z. Li, S.Y. Li, and Y.A. Chen, Hot deformation behavior of Fe–27.34Mn–8.63Al–1.03C lightweight steel, *Int. J. Miner. Metall. Mater.*, 30(2023), No. 4, p. 734.

[54] M.J. Wang, W.R. Wang, Z.L. Liu, C.Y. Sun, and L.Y. Qian, Hot workability integrating processing and activation energy maps of Inconel 740 superalloy, *Mater. Today Commun.*, 14(2018), p. 188.

[55] J.H. Zhao, Y.L. Deng, F.S. Xu, and J. Zhang, Effects of initial grain size of Al–Zn–Mg–Cu alloy on the recrystallization behavior and recrystallization mechanism in isothermal compression, *Metals*, 9(2019), No. 2, art. No. 110.

[56] P. Wang, T.H. Yin, and S.X. Qu, On the grain size dependent working hardening behaviors of severe plastic deformation processed metals, *Scripta Mater.*, 178(2020), p. 171.

[57] A. Tiamiyu, V. Tari, J. Szpunar, A. Odeshi, and A. Khan, Effects of grain refinement on the quasi-static compressive behavior of AISI 321 austenitic stainless steel: EBSD, TEM, and XRD studies, *Int. J. Plast.*, 107(2018), p. 79.